

Hybrid Transparent PEDOT:PSS Molybdenum Oxide Battery-like Supercapacitors

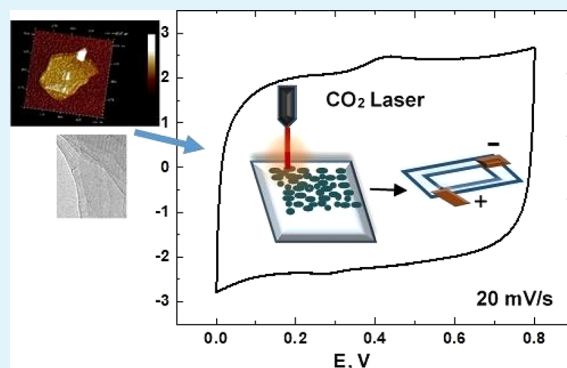
Mitra Yoonessi,^{*,†,‡,§} Arie Borenstein,[†] Maher F. El-Kady,[†] Christopher L. Turner,[†] Haosen Wang,[†] Adam Z. Stieg,[§] and Laurent Pilon^{‡,§}

[†]Department of Chemistry and Biochemistry, [‡]Department of Mechanical and Aerospace Engineering, and [§]California NanoSystems Institute, University of California, Los Angeles (UCLA), Los Angeles, California 90095, United States

S Supporting Information

ABSTRACT: We report fabrication of flexible all-solid-state transparent electrochromic patterned microsupercapacitors based on two-dimensional layered nanostructured molybdenum oxide (MoO_{3-x})/poly(3,4-ethylenedioxythiophene)–polystyrenesulfonate (PEDOT:PSS) nanocomposite electrodes. Exceptional electrochemical performance of the transparent microsupercapacitors includes fast kinetics and response times, high specific capacitances (up to 79.2 C/g, 99 F/g, and 2.99 mF/cm²), and Coulombic efficiencies of 99.7% over 2500 cycles. Such exceptional performance is attributed to the synergistic effects of PEDOT:PSS providing high electrical conductivity and high charge storage capacity along with its segregated interfacial nanostructure facilitating the intercalation of the ionic species, H^+ (Na^+ , K^+) and SO_4^{2-} , into the high surface area tunnel structure of the 2D MoO_{3-x} nanosheets. Supercapacitors using MoO_{3-x} PEDOT:PSS electrodes exhibit optical transmittance above 70% ($\lambda = 380\text{--}730$ nm). The electrochromic performance of the transparent microsupercapacitor is due to both PEDOT:PSS and cation (H^+) intercalation in the tunnel structure of MoO_{3-x} .

KEYWORDS: transparent supercapacitor, 2D materials, PEDOT:PSS, molybdenum oxide nanoparticles, nanocomposite electrode, electrochromic



INTRODUCTION

Advanced electrochemical capacitors require high power density, excellent charge storage capability, fast response time, safety, cycle life, and large energy density.^{1–12} Recent requirements for embedded energy storage systems are small, thin, lightweight, and flexible yet high specific capacitance, high energy, and power density.^{1–12} Transparent thin film solid-state flexible supercapacitors are currently under intense investigation for optoelectronics applications.^{14–21} The combination of transparency, electrical conductivity, charge storage capacity, the capability of undergoing redox (and/or intercalation) reactions, and electrochemical stability is extremely difficult to achieve. Optically transparent pristine 1–2 layer thin graphene supercapacitors featured an areal capacitance of 80 μFcm^{-2} while multilayer graphene oxide demonstrated 394 μFcm^{-2} .¹⁴ Hierarchical Ag–Au nanomaterials have been utilized in transparent supercapacitors exhibiting 136.5–209.9 $\mu\text{F/cm}^2$.¹⁶ Transparent stretchable supercapacitors of wrinkled graphene have shown 57% transparency at 550 nm with areal capacitance of 5.8 $\mu\text{F cm}^{-2}$ and gravimetric capacitance of 7.6 F g^{-1} .¹⁵ Highly stretchable transparent supercapacitors based on Ag–Au core–shell nanowires showed areal capacitance up to areal capacitance of 209.9 $\mu\text{F/cm}^2$.¹⁷ Pseudocapacitor transparent

ruthenium oxide aerogel-based supercapacitors with loading 51 levels of 16.3 $\mu\text{g cm}^{-2}$ exhibited gravimetric capacitance of 52 79.6, 79.2, 75.9, and 72.3 F g^{-1} and areal capacitances of 1.30, 53 1.29, 1.23, and 1.18 mF cm^{-2} at scan rates of 25, 50, 75, and 54 100 mV s^{-1} .¹⁹ Recently, all-solid-state highly stretchable, 55 transparent, and flexible electrodes of graphene PEDOT:PSS 56 microsupercapacitors showed an excellent performance of 790 57 $\mu\text{F cm}^{-2}$ at the discharge current of 50 $\mu\text{A cm}^{-2}$.²¹ 58

Transition metal oxides provide opportunities for the next 59 generation of optoelectronics and electrical energy storage 60 systems due to their exceptional electrical properties, optical 61 band gap, and high surface area for intercalation/deintercalation 62 of ionic species.^{4,22–28} Transparent supercapacitors 63 require high transparency, good electrical conductivity, and 64 large charge storage capacity. Two-dimensional materials such 65 as graphene and transition metal dichalcogenides (e.g., MoS_2 , 66 MoTe_2 , MoSe_2 , WS_2 , and MoO_x) are excellent potential 67 candidates for advanced optoelectrochemical storage devi- 68 ces.^{4,22–28} Charge carriers in graphene travel essentially with 69 massless speed of light electron transport ($c^* \approx 10^6 \text{ m s}^{-1}$) in 70

Received: December 28, 2018

Accepted: May 30, 2019

Published: May 30, 2019

71 the absence of scattering.²⁹ Although a graphene single layer is
72 97% transparent with respect to the incident beam, chemically
73 derived reduced graphene exists in multiple layers and stacks,
74 making the >90% optical transparency required for optoelec-
75 trical devices difficult to achieve. The 2D transition metal
76 dichalcogenide MoO_{3-x} family has tunable optical and
77 electrical properties which can be readily tailored, making
78 them of great interest for transparent energy storage
79 devices.^{4,22–28}

80 Molybdenum oxide has a wide range of optical and electrical
81 properties which are dependent on its oxidation state (Mo^{2+} ,
82 Mo^{3+} , Mo^{4+} , Mo^{5+} , and Mo^{6+}), dopants, doping level, and
83 crystal structure.^{4,22–28} MoO_3 has a large work function (6.6
84 eV) due to its closed shell structure.²⁷ Shallow oxygen
85 vacancies in MoO_3 make it an n-type degenerate semi-
86 conductor that can easily donate electrons.^{25–28} This makes
87 MoO_3 ideal for proton (H^+ or Li^+) intercalation, resulting in
88 high electrical conductivity suitable for energy storage devices
89 such as pseudocapacitors. Molybdenum oxides have excep-
90 tional electrochemical properties due to their tunnel structures
91 created from MoO_6 octahedra, where Li^+ and H^+ ions can be
92 readily intercalated and deintercalated.^{25–28} As a result of
93 proton intercalation, the electrical conductivity of MoO_3
94 increases.^{4,25–28} Kalantarzadeh et al. proposed the H^+ can
95 intercalate in the oxygen of MoO_3 , resulting in a significant
96 increase in free electron concentration.^{23,26} It has been also
97 reported that hydrogen insertion causes extended lattice
98 distortion in $\alpha\text{-MoO}_3$, resulting in a significant reduction of
99 the energy gap.^{23–28} Simulations predicted any n-type electron
100 doping or charge transfer results in band gap distortion.^{23–28}
101 Huang et al. reported proton intercalation significantly deforms
102 $\text{O}_2\text{-Mo-O}_2$ chains, leading to band gap narrowing and optical
103 band gap reduction.^{25–27} The intrinsic conductivity of fully
104 oxidized MoO_3 has been reported as 10^{-5} S/cm² and increased
105 to 10^{-4} S/cm for reduced MoO_3 .⁴ Because of its limited
106 electrical conductivity, molybdenum oxide is used in
107 composite structures with highly conductive additives such as
108 activated carbon or graphene.^{23–28} Molybdenum oxides and
109 their nanocomposites have shown excellent performance as
110 supercapacitors where active material loading can be high and
111 there is no transparency requirement.^{30–33} Supercapacitors
112 with MoO_3 -graphene composite electrodes demonstrated a
113 capacitive performance of 148 F/g by using aqueous
114 electrolyte of 1 M Na_2SO_4 .^{30–33} Despite reports of MoO_3
115 supercapacitors,^{30–33} to the best of our knowledge, there is no
116 report of an organic-inorganic PEDOT:PSS molybdenum
117 oxide nanocomposite as a transparent microsupercapacitor
118 electrode.

119 Acid-based electrolytes, such as sulfuric and phosphoric acid,
120 have been incorporated in a network of poly(vinyl alcohol)
121 (PVA) gels to generate all-solid-state supercapacitors where
122 safety, low toxicity, and flexibility are important criteria.³⁴
123 Supercapacitors of interwoven carbon nanotubes (CNTs)
124 embedded in polydimethylsiloxane (PDMS) featured a
125 capacitance per unit footprint of 0.6 mF/cm² in KOH solution
126 compared to 0.3 mF/cm² in KOH gel electrolyte.³⁴ The $\text{p}K_a$ is
127 the ionic dissociation strength; the ionic dissociation and ion
128 diffusion in macromolecular gels are more complex and have
129 been modeled as a function of chemical potential of ionic
130 species, flux vectors, diffusivities and concentrations of ionic
131 species, and temperature as a three-dimensional network when
132 an electric field was applied.^{35,36}

PEDOT:PSS is a transparent conductive polymer with both
good electrical and ionic conductivity and a theoretical
capacitance of 210 F/g.^{37–41} The origin of the PEDOT:PSS
complex ionic-electrical coupling has been investigated by
describing the cyclic voltammogram using a 2D Poisson-
Nernst-Planck analysis.^{37–41} The high capacitance has been
attributed to the high surface area phase-separated morphology
and to a large contribution of the electric double layer (EDL)
formation along the interfaces between the electron conduct-
ing PEDOT and ion-transporting PSS.^{37–41} The charge storage
capacity is also enhanced by the free volume of PEDOT.
Sulfuric acid-doped PEDOT:PSS exhibits 4 times higher
electrical conductivity (4380 S cm^{-1}), improved transparency,
increased crystallinity, and a change in morphology to a fibrillar
structure with an enhanced surface area.^{37–41}

Recently, all conjugated electrochromic supercapacitors
based on polyaniline capacitive coating and electrochromic
conjugated polymers demonstrated dual functionality promis-
ing potential for smart windows.⁴² Metal oxides such as
tungsten oxide (WO_3), niobium oxide (Nb_2O_5), and titanium
dioxide (TiO_2) have shown electrochromic behavior where
anodic electrochromism is reported for nickel oxides and
special vanadium pentoxide.^{42–44} Self-powered electrochromic
nanogenerators with an average visible optical modulation
(ΔT_{vis}) of 15.3% and a response time of 10 s have been
recently reported.^{42–44} PEDOT:PSS silver grid films were
coated with electrochromic WO_3 to generate flexible hybrid
structure with large optical modulation (81.9% at 633 nm), fast
switching, and high coloration efficiency ($124.5 \text{ cm}^2 \text{ C}^{-1}$).⁴⁵

In this study, we report a solid-state hybrid organic-
inorganic PEDOT:PSS- MoO_3 transparent supercapacitor
device prepared in a facile, yet scalable method. We designed
all-solid-state flexible thin transparent pseudocapacitor electro-
des based on 2D nanosheet stacks of an orthorhombic (o)-
 MoO_3 /PEDOT:PSS hybrid structure with a poly(vinyl
alcohol)-sulfuric acid (PVA-SA) gel electrolyte. These
microsupercapacitors were prepared in two configurations:
an interdigitated pattern and a window and frame design using
a CO_2 ($\lambda = 10.6 \mu\text{m}$) laser patterning method. The
microsupercapacitors exhibited excellent electrochemical per-
formance with high specific capacitances up to 79.2 C/g, 99 F/
g, and 2.99 mF/cm² as well as Coulombic efficiencies of 99.7%
over 2500 cycles. The device performance is attributed to the
high surface area fibrillar morphology of the sulfuric acid-
doped PEDOT:PSS, enabling high charge storage capacity
(H^+ , SO_4^{2-}) which makes the charges readily available for
intercalation into the tunnel structure of the o- MoO_{3-x} .

EXPERIMENTAL SECTION

Materials. Molybdenum(II) acetate dimer (Alfa Aesar), poly(vinyl
alcohol), acetone, and NMP (Sigma-Aldrich) were used as received.
PEDOT:PSS-coated PET films were generously donated by Kimoto
Tech.

Molybdenum Oxide Synthesis. Molybdenum(II) acetate dimer
(MoAD) was used as an organometallic precursor. In a typical
preparation method, 0.25–1 mmol of MoAD was dissolved in 3–5
cm³ of NMP and then added dropwise to the anhydrous NMP
solution at 190 °C while stirring under nitrogen. The dispersion was
stirred at 190 °C for 15 min, 30 min, 45 min, and 1 h. The resultant
dispersion was centrifuged and washed with acetone three times until
clear. Subsequently, the resulting nanoparticles were annealed at 400
°C to yield light blue nanoparticles.

**Fabrication of the Flexible All-Solid-State Supercapacitors:
Electrode Preparation.** The molybdenum oxide nanoparticles were

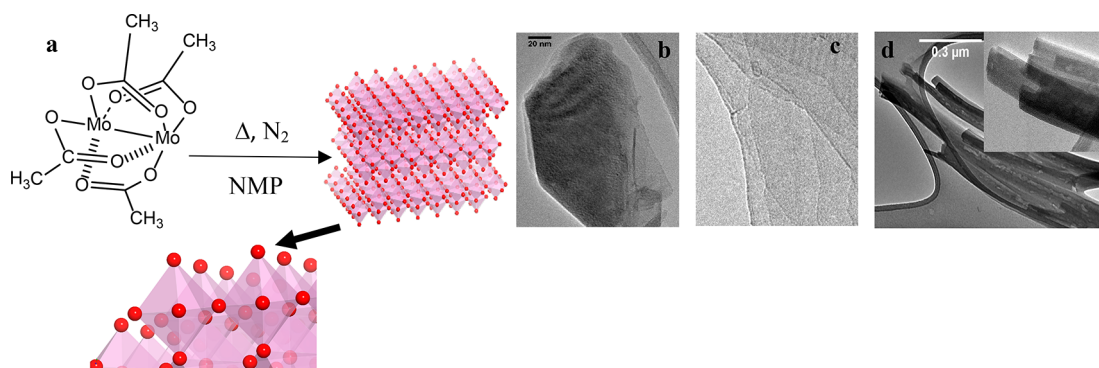


Figure 1. (a) A reaction scheme for molybdenum acetate dimer in NMP forming MoO_3 on heating at 195°C followed by annealing at 400°C . (b) TEM micrograph of a typical MoO_3 nanoparticle. (c) At higher TEM magnification a stack of MoO_3 nanosheets appears to be semitransparent under the electron beam. (d) TEM micrograph of MoO_3 nanoscrolls.

196 dispersed in acetone (0.01 g/l cm^3 acetone) and spray-coated using
 197 an airbrush onto a set of PEDOT-coated PET current collectors.
 198 Transparent current collectors with PEDOT:PSS had a thicknesses of
 199 $\sim 0.45\ \mu\text{m}$ and a nominal surface resistivity of $200\ \text{ohm/sq}$. The spray-
 200 coating was performed on a hot plate set at a temperature of 55°C
 201 with a total weight of $0.08\text{--}0.15\ \text{mg}$ ($0.04\text{--}0.075$ per electrode) on a
 202 $1\ \text{cm} \times 1\ \text{cm}$ square area of electrode. After drying, the electrodes
 203 were patterned by using a CO_2 laser in two configurations: a window
 204 and frame pattern and a three-finger interdigitated pattern. The
 205 separation between the electrodes was $0.9\text{--}1\ \text{mm}$. Poly(vinyl alcohol)
 206 (PVA)–sulfuric acid gel was used as the gel electrolyte. The devices
 207 were covered with a second PET sheet to minimize water evaporation
 208 and the presence of oxygen.

209 ■ RESULTS AND DISCUSSION

210 **Fabrication and Characterizations of o- MoO_3 Nanoparticles.** We developed a solvent-based syn-
 211 thesis method to prepare two-dimensional o- MoO_3 nanosheets
 212 and/or nanoscrolls examined using high-resolution trans-
 213 mission electron microscopy (HR-TEM) (Figure 1a–d). The
 214 chemical and crystalline structure and the morphology of the
 215 molybdenum oxide nanosheets were characterized by using
 216 wide-angle X-ray scattering (WAXS), X-ray photoelectron
 217 microscopy (XPS), atomic force microscopy (AFM), and high-
 218 resolution microscopy (HR-TEM). The crystalline structures
 219 of the MoO_3 nanosheets and nanoscrolls were determined to
 220 be orthorhombic by using WAXS (Figure 2).^{46–48} During this
 221 reaction, Mo^{4+} atoms of molybdenum(II) acetate dimer
 222 (MoAD) were oxidized from Mo^{4+} to Mo^{6+} and Mo^{5+} . The
 223 resultant o- MoO_3 nanosheets had a small atomic percent of
 224 Mo^{5+} in addition to Mo^{6+} , leading to a higher conductivity and
 225 enhanced electrochemical performance (WAXS, AFM, and
 226 XPS, Figures 2–5). The molybdenum acetate dimer precursor
 227 was oxidized to o- MoO_{3-x} in *N*-methyl-2-pyrrolidone (NMP)
 228 at 190°C followed by thermal annealing at 400°C (Figure
 229 1a). At higher temperatures once the carbon species bonded to
 230 the oxygen atoms were decomposed, the oxygen atoms were
 231 oxidized from Mo^{4+} to Mo^{5+} and Mo^{6+} . An inert atmosphere
 232 was used to limit the availability of free oxygen atoms and
 233 molecules to generate reduced MoO_3 . This resulted in a light
 234 blue color for o- MoO_3 after annealing. The o- MoO_3 consists of
 235 stacks of two-dimensional nanosheets forming nanoparticles. A
 236 typical o- MoO_3 nanoparticle with lateral dimensions of $190\ \text{nm}$
 237 $\times 100\ \text{nm}$ consisting of o- MoO_3 nanolayers and stacks is
 238 shown in Figures 1b,c and 3a–c. The single or few nanosheets
 239 of o- MoO_3 appear to be nearly transparent with respect to the
 240 incident beam and have a tendency to fold at the edges of
 241

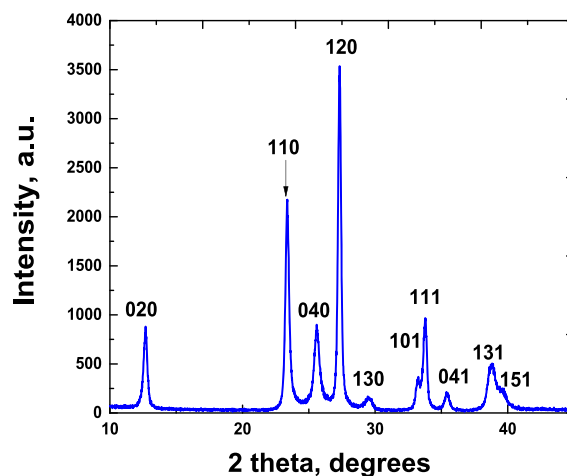


Figure 2. Wide-angle X-ray diffraction pattern of the molybdenum oxide nanoparticles indexed to orthorhombic MoO_3 (JCPDS 01-089-5108).

single or few layer nanosheets. The particle size distribution 242
 determined by dynamic light scattering features lateral 243
 dimensions ranging from $60\ \text{nm}$ to $1.6\ \mu\text{m}$, with an average 244
 particle size of $339 \pm 166\ \text{nm}$ (Table S1). The single or few 245
 nanolayers of o- MoO_3 are extremely thin and nearly 246
 transparent with respect to the incident electron beam (HR- 247
 TEM, Figures 1c and 3a–c). This indicates that the 2D layered 248
 structure materials can be exfoliated to atomically thin single 249
 layer (or few layers) of low color MoO_3 which makes them 250
 ideal for transparent supercapacitors. The thin layered 251
 structure of MoO_3 has excellent optical properties and low 252
 absorption in the visible wavelength range. The optical 253
 transparency of composite layers of MoO_3 thin layer and 254
 silver layer deposit is reported as 70% normal transmittance in 255
 the wavelength range of $350\ \text{nm} < \lambda < 550\ \text{nm}$.⁴⁹ The two- 256
 dimensional layered structure of MoO_3 that can be readily 257
 exfoliated into single and few atomic thin layers provides an 258
 excellent opportunity for their application in transparent 259
 energy storage devices. The 2D layered nanosheet structure 260
 of the o- MoO_3 results in a high surface area per nanoparticle 261
 and is ideal for EDL charge storage and ion intercalation. 262

The X-ray diffraction pattern was matched with JCPDS 01- 263
 089-5108, indicating an orthorhombic MoO_3 structure.^{46–48} 264
 The orthorhombic MoO_3 structure consists of edge and 265
 corner-sharing MoO_6 with a unit cell of $a = 3.962\ \text{\AA}$, $b = 266$

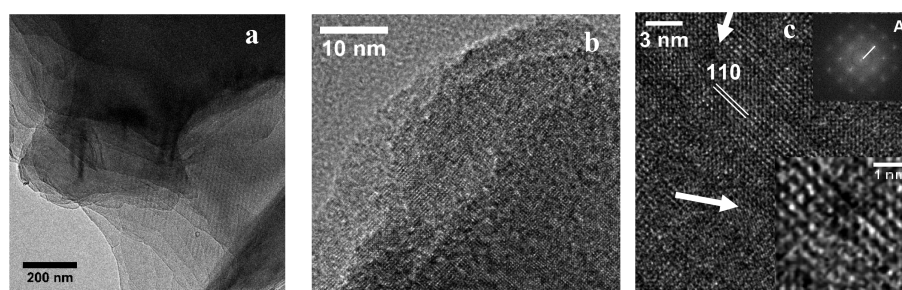


Figure 3. (a) Layered structure of the MoO₃ nanoparticles. (b) High-resolution images of the synthesized MoO₃ nanoparticles showing the lattice fringes in the stacked nanosheet structure. (c) The FFT of the image shows the 110 plane (at point A, 3.8 Å). Atomic structure of the molybdenum and oxygen in the planar structure are presented.

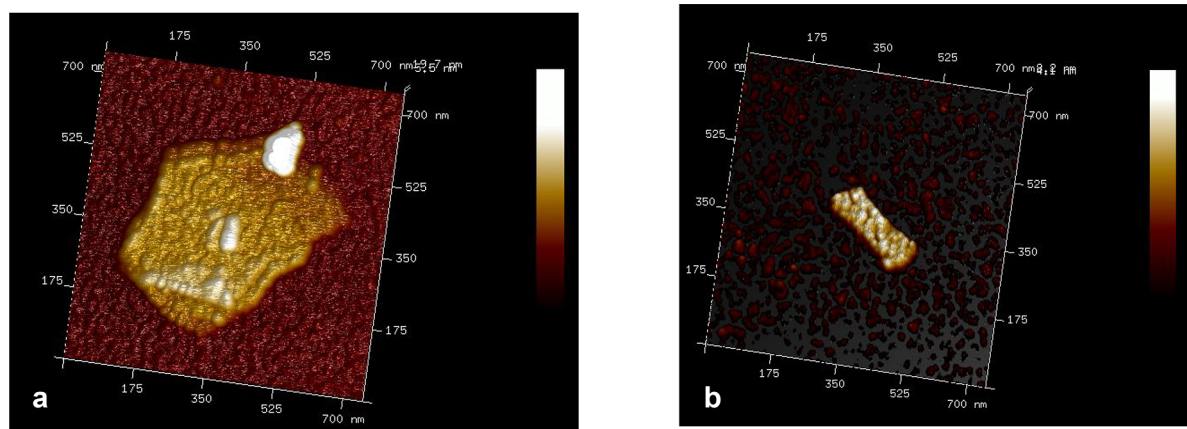


Figure 4. Topography of MoO₃ measured by AFM for a layered particle deposited on Au-coated sapphire. (a) Larger stack of MoO₃ particle (408 × 532 nm²). (b) Nanosheet of MoO₃ (238.5 × 71.9 nm²).

267 13.855 Å, and $c = 3.701$ Å. The Scherrer equation ($\tau = K\lambda/\beta$
 268 $\cos \theta$) was used to calculate the mean crystallite size (t) by
 269 using the full width half-maximum (peak broadening, b), taking
 270 into account the instrument broadening constant ($K = 0.94$),
 271 wavelength $\lambda = 1.5418$ Å, and the peak position (θ) Rietveld
 272 refinement using the least-squares minimization approach for
 273 fitting the shape of the measured peak profile to the calculated
 274 one based on the wave vector diffraction principle ($q = 4\pi$
 275 $\sin(\theta)/\lambda$) in reciprocal space ($q =$ wave vector) for crystal unit
 276 cell calculations.^{47,48} This refinement resulted in cell unit
 277 parameters of $a = 3.965$ Å, $b = 13.79$ Å, and $c = 3.72$ Å and
 278 space group of pnm (shown in the Supporting Information).

279 The complete list of values, lattice spacing, crystallite size,
 280 and unit cells from both Scherrer calculations and Rietveld
 281 refinement are listed in Table S2. The Scherrer calculation
 282 values are the crystallite size, which is different from particle
 283 size. This approximation is well within the validity range of the
 284 Scherrer equation (<100 nm). X-ray diffraction patterns
 285 indicate that the orthorhombic MoO₃ structure consists of
 286 edge and corner-sharing MoO₆ octahedra with crystallite sizes
 287 ranging from 31.3 to 76.2 nm in different lattice (hkl) planes,
 288 040 and 021, respectively, based on the Scherrer equation
 289 (Figure 2 and Table S2).^{46–48} The crystallite's shape could be
 290 approximated as spherical, as indicated by the absence of
 291 asymmetric peak broadening.

292 To further investigate the morphology of the two-dimen-
 293 sional MoO₃ nanoparticles, high-resolution TEM and AFM
 294 were utilized (Figures 3 and 4). High-resolution micrographs
 295 of MoO₃ nanosheets show the growth of o-MoO₃ in the 110
 296 direction with a lattice spacing of 3.8 Å (Figure 3a–c). The

high-resolution micrograph confirms thin layers of o-MoO₃
 with a wavy and wrinkled structure; the nanosheets are prone
 to rolling up and forming tubular structures. The fast Fourier
 transform of the MoO₃ micrographs confirms the lattice
 spacing as 3.8 Å in the 110 direction.

The AFM images of the o-MoO₃ show the thin layers of the
 highly exfoliated particles with height ranging measured
 between 1.3 and 26 nm (Figure 4a,b). The exfoliated o-
 MoO₃ nanolayers were prepared by dispersing the particles in
 the mixture of acetone and alcohol followed by sonication and
 drop-casting from a dilute dispersion on Au-coated sapphire.
 The exfoliation protocol was followed closely to the protocol
 used for generating the MoO₃ aerosol for electrode
 preparation. The o-MoO₃ nanosheets were flexible and
 conformed to the gold substrate morphology. A stack of
 MoO₃ nanosheets (408 × 532 nm²) with a height of ~9 nm
 with the top nanosheet rolled up can be observed in Figure 4a.
 Figure 4b demonstrate a MoO₃ nanosheet (238.5 × 71.9 nm²)
 with a height of 3.13 nm.

The Raman spectra exhibit peaks at 996, 818, 666, 244, 290,
 and 337 cm⁻¹ due to o-MoO₃ (shown in the Supporting
 Information).^{4,23–28} High-resolution XPS peak deconvolution
 shows a peak at 232.5 eV corresponding to Mo⁶⁺ (Mo 3d_{5/2})
 with a contribution from a peak at 231.2 eV corresponding to
 Mo⁵⁺ 3d_{5/2} (Figure 5).^{4,23–28} The separation of the Mo 3d_{5/2}
 and Mo 3d_{3/2} doublet was ~3.1 eV, confirming the presence of
 Mo⁶⁺ in MoO₃. The smaller peak at a lower binding energy of
 231.2 eV is due to a lower oxidation state slightly reduced
 MoO₃. The ratio of Mo 3d_{5/2} to Mo 3d_{3/2} peaks was ~3:2, in
 good agreement with the binding energies and area ratios 326

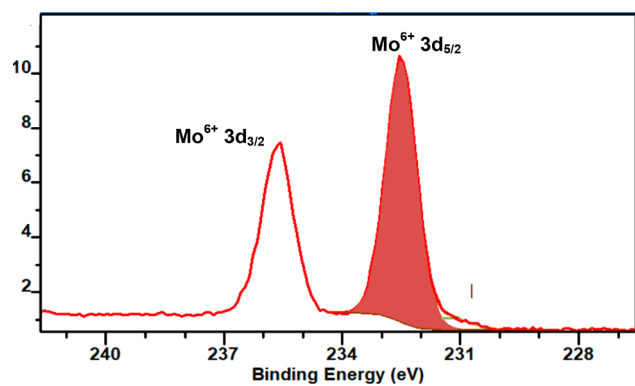


Figure 5. High-resolution XPS spectra of Mo of the MoO_3 showing Mo^{6+} and some contribution of Mo^{5+} .

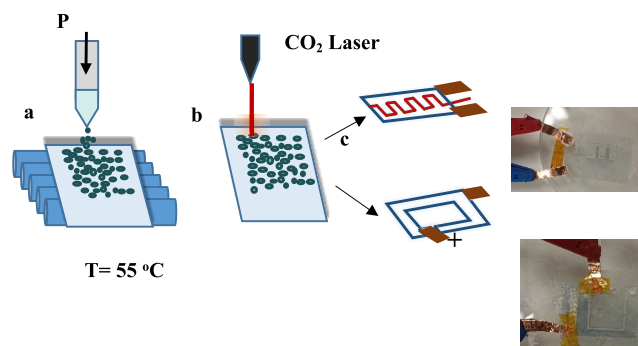


Figure 7. A dispersion of o-MoO_3 nanosheets was air-brushed onto the PEDOT:PSS PET films followed by laser patterning to form the electrodes. (a) A dispersion was spray-coated using a high-pressure nozzle. (b, c) The coated films were dried and laser patterned by using a CO_2 laser. (d) Fabricated devices exhibited electrochromic and blue color in negative electrode when voltage was applied.

PEDOT:PSS PET films (Figure 7a,b). Then, the composite electrodes were patterned by using a CO_2 laser ($\lambda = 10.6 \mu\text{m}$) into interdigitated patterns or window and frame configurations. The devices were designed using 2D molybdenum oxide nanoparticles and PEDOT:PSS, which both contribute to the capacitance, while PEDOT:PSS also acts as a current collector. This processing method has the advantage of facile scale up to roll-to-roll processing.

Device Characterization. The transmittance of visible light ($\lambda = 380\text{--}730 \text{ nm}$) through the PEDOT:PSS films and through the PET/PEDOT:PSS/ o-MoO_3 /sulfuric acid gel devices was measured (Figure 8). The transparency of the

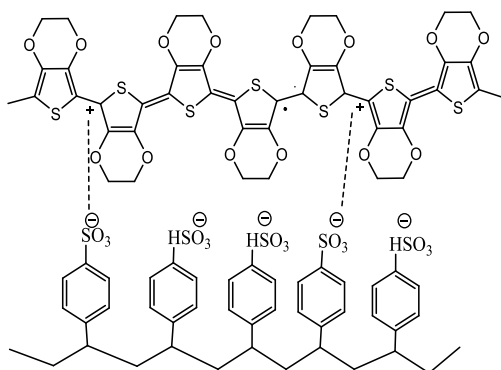


Figure 6. Schematic of the chemical structure of PEDOT:PSS.

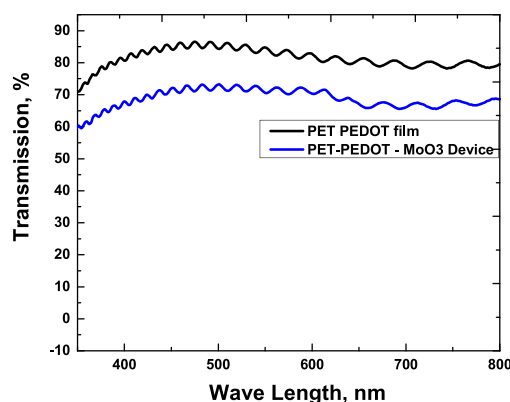


Figure 8. Transmittance of visible light ($\lambda = 450\text{--}750 \text{ nm}$) for an MoO_3 /PEDOT:PSS/PET device compared with a PEDOT:PSS/PET film. The interference fringes are due to the thin film of PEDOT:PSS coated on the PET surface.

supercapacitors is evident in Figure 8 where average transmittances of $>70\%$ can be seen in the visible region. The o-MoO_3 particle size and particle dispersion can affect the light transmission and scattering especially if large aggregates form. The oscillations observed in the spectra are due to interference fringes from the thin PEDOT:PSS coating (520 nm in thickness).

The device exhibited a color change on the negative electrode, while the positive electrode remained transparent. In the window and frame configuration, the frame is the negative electrode and the window center is the positive electrode. The color change of the negative electrode is attributed to two

reported for o-MoO_3 .⁴ The higher conductivity and pale blue color of the synthesized o-MoO_{3-x} are in agreement with slightly reduced MoO_3 approximated as $\text{MoO}_{3-0.05}$ (based on the area ratio of $\text{Mo}^{5+}/\text{Mo}^{6+}$). The presence of lower oxidation states (Mo^{5+} , Mo^{4+}) has been associated with increased electrical conductivity and electrochemical activity.⁴

Device Fabrication. PEDOT:PSS is a conductive polymer with a mixed mode of electrical and ionic conductivity (Figure 6) that has been used both as an active material and as a

transparent current collector. PEDOT:PSS has a phase-segregated morphology. PEDOT:PSS forms a crystalline solid, and the degree of crystallinity increases with sulfuric acid doping.^{37–41} Studies have shown that the increase in sulfuric acid doping results in high electrical conductivity reaching σ_{dc-max} of 4380 S/cm at 100% sulfuric acid doping, while maintaining a high level of transparency comparable to that of indium tin oxide (ITO).^{37–41} Therefore, based on reports on doping PEDOT:PSS with PVA sulfuric acid electrolyte, a high electrical conductivity can be achieved, along with a fibrillar highly phase-separated morphology which generates high surface area and improved transparency.^{37–41} This will facilitate charge storage (H^+ , SO_4^{2-}) via intercalation into the tunnel structure of o-MoO_3 . To further process and form the electrodes, the o-MoO_3 stacked nanosheets were dispersed in acetone and sonicated for 15 min before using a high-pressure spray-coater to create PEDOT:PSS-coated PET films (Figure 7). This method promotes dispersion of the layers and maximizes the surface area. The dispersions were applied using an air brush which even promotes finer aerosols, resulting in a more uniformly dispersed nanoparticles on the

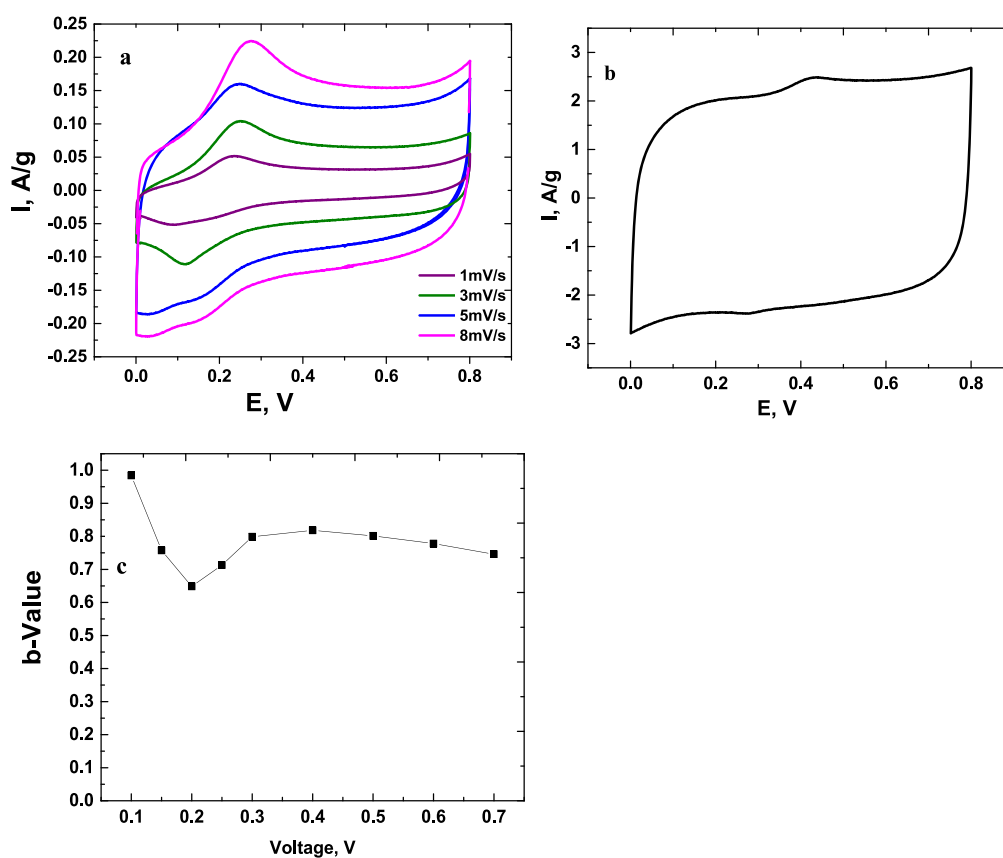


Figure 9. Electrochemical performance of the transparent supercapacitor. (a) Cyclic voltammogram of the MoO₃/PEDOT:PSS/PET device measured at 1, 3, 5, and 8 mV/s clearly showing a redox peak. (b) Cyclic voltammogram of the MoO₃/PEDOT:PSS/PET device at 20 mV/s showing a larger contribution of the EDL. (c) The b values were calculated from the power-law dependence of the current to the scan rate.

phenomena: (1) the intercalation of protons into the tunnel structure of o-MoO₃ upon application of a voltage and (2) the electrochromic response of PEDOT:PSS. The positive electrode remains nearly transparent likely because the negative ions (HSO₄⁻, SO₄²⁻) are too large for intercalation within the MoO₃ crystal structure. Electrochromic energy storage devices can be used in smart windows with dual functionality of energy storage capability.

Electrochemical Measurements. The main parameters of microsupercapacitor performance are (1) high specific capacitance, (2) fast charge/discharge rates, (3) efficiency and cyclability, (4) safety, (5) flexibility, and (6) facile production, i.e., low cost. Cyclic voltammetry of a typical transparent supercapacitor device (two identical electrodes, 0.9–1 mm nonconductive separator in PVA–SA gel electrolyte) in the sweeping voltage range from 0 to 0.8 V and scan rates of 1, 3, 5, and 8 mV/s is presented in Figure 9a. The current increased immediately as the voltage was increased followed by a redox peak showing nearly ideal supercapacitor behavior with excellent rate capacity. The discharge was rapid and exhibited a reverse peak, indicating reversible redox activity. It has been reported that molybdenum oxide-based supercapacitors show an irreversible peak Li⁺ ion intercalation in the first cycle.⁴ The first cycle in the molybdenum oxide:PEDOT:PSS supercapacitors exhibited an irreversible peak which was not taken into account for the measurements and calculations. The devices demonstrated electrochromic behavior. Once the voltage was applied, the negative electrode color changed to a darker blue, while the positive electrode remained trans-

parent. This response is indicative of mixed redox and ion diffusion activities. Both PEDOT:PSS and o-MoO₃ are electrochemically active; therefore, the presence of redox peaks indicates the electrochemical response of both PEDOT:PSS and H⁺ intercalation into the tunnel structure of o-MoO₃. Diffusion-controlled H⁺ insertion occurs at low scan rates where the time scale of the processes allows ion diffusion in the inner structure of the o-MoO₃ (Figure 9a,b).

The capacitive response changed to EDLC type when the scan rate was increased to 20 mV/s, where the fast scan rate does not provide enough time for redox reactions and intercalation and deintercalation of protons (H⁺) into the tunnel structure of o-MoO₃ (Figure 9b). The majority of the capacitive contribution can be attributed to EDLC formation in the two-phase structure of PEDOT.^{37–41} The charge storage mechanism was evaluated by fitting the change of the current, $I(v)$, as a function of scan rate v at a specific voltage (V) to a power law: $I(v) = av^b$ (Figure 9c).^{51–56} The b value variations are indicative of Faradaic and non-Faradaic currents. When the b value is close to 1, this indicates capacitive control, while a b value close to 0.5 indicates diffusion-controlled currents. Figure 9c shows b values close to 1 at low voltage (0.1 V) followed by a sudden decrease to 0.64 at 0.2 V, indicative of diffusion-controlled reactions at low voltage (\sim 0.2 V). The b value then increased to \sim 0.8 above 0.4 V, indicating that the charge storage mechanism is now dominated by the electric double layer formation at higher voltage. The change in b value in this system is an indication of mixed intercalation, redox, and EDLC currents.^{51–56} The Faradaic reactions occur at low

439 voltage while the performance quickly changes to EDLC at
440 slightly higher voltages.

441 The gravimetric capacitance (C_g , F/g), the specific
442 capacitance (C_s , C/g), and the footprint areal capacitance (C_a
443 in mF/cm²) were calculated from the CV curves at each scan
444 rate (eqs S1 and S2) (Figure 9a,b). The gravimetric
445 capacitance (and specific capacitance) values are 99.8 F/g
446 (79.8 C/g), 95.0 F/g (76 C/g), 90.4 F/g (72.3 C/g), and 86.8
447 F/g (69.4 C/g) at scan rates of 1, 3, 5, and 8 mV/s,
448 respectively. The footprint areal capacitance values are 3.0, 2.9,
449 2.7, and 2.6 mF/cm² at scan rates of 1, 3, 5, and 8 mV/s,
450 respectively. The gravimetric and areal capacitance values are
451 high, and the device maintained its capacitance within the
452 examined scan rate range (Figure 10). Dai et al. reported

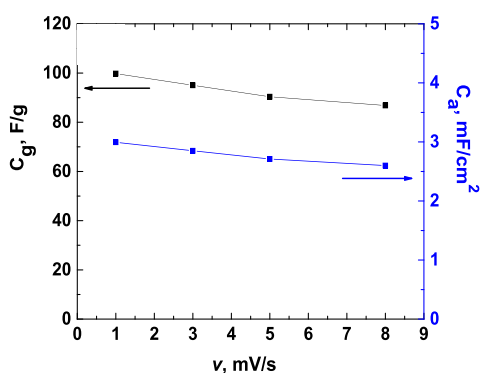


Figure 10. Electrochemical performance of the transparent supercapacitor of calculated specific capacitance (C_g and C_a) as a function of scan rates.

453 specific capacitance of 29.2 F/g for long CNT polydimethylsi-
454 loxane stretchable transparent supercapacitors.⁵⁷ Transparent
455 flexible solid-state supercapacitors of graphene electrodes with
456 phosphoric acid gel electrolyte exhibited 12.4 μ F/cm² at 10
457 mV/s.¹⁸ Our device offers high specific capacitances (up to 99
458 F/g, 2.99 mF/cm²), and Coulombic efficiencies of 99.7% over
459 2500 cycles exceeding the performance of the transparent
460 supercapacitors with transparency higher than 70% at 550 nm
461 reported in the literature.^{14–21}

The Nyquist plot (Figure 11a) shows a semicircle followed
by a diffusion-related impedance and then a change of Z' to
almost parallel to $-Z''$ at low frequencies indicating nearly
ideal supercapacitive behavior. The resistance at high
frequency due to contact resistance was negligible (A in
Figure 11a). The PEDOT:PSS acts as both a current collector
and an active material; therefore, there is essentially no contact
resistance. The electrode resistance was negligible compared to
the bulk electrolyte, mass transfer, and charge transfer
resistances. The semicircle resistance (B) represents a
combination of the bulk electrolyte, mass transfer, and charge
transfer resistances of 838.2 Ω , in reasonable agreement with
that calculated from the IR drop as $766.6 \pm 14.4 \Omega$. This high
value is likely due to the high resistance of the gel electrolyte.
The low-frequency Warburg impedance at 45 $^\circ$ C can be
attributed to diffusion processes.³ A linear fit of Z' vs $\omega^{-1/2}$
(frequency < 25 Hz) resulted in a Warburg coefficient (σ) of
 $357 \pm 58 \text{ ohm}^{0.5}$ (Figure 11b).³ This value is higher than
comparable low-viscosity electrolyte devices, likely due to slow
diffusion of the ions through the high-viscosity PVA gel.

The Bode plot shows two step changes: one at high-
frequency (~ 632.9 Hz) followed by a second at lower
frequency (0.06 Hz) (shown in the Supporting Information).
This resulted in a 2.8 s response time (at a phase angle of
 -45°), indicating a complex electrochemical activity with a
contribution from both capacitive moieties—PEDOT:PSS and
o-MoO₃—affecting the electrochemical activities of the
supercapacitor. The fast response time of the device can be
attributed to the fast kinetics of proton intercalation/
deintercalation in the tunnel structure of o-MoO₃. Hydrogen
doping decreases the MoO₃ bandgap, expands and contracts its
lattice structure upon intercalation and deintercalation, and
changes its color.^{21–24} PEDOT:PSS has also been reported as
an electrochromic material. Doping PEDOT:PSS with sulfuric
acid results in a nanofibrillar segregated PEDOT structure with
high surface area which can store charge (H^+ and SO_4^{2-}) and
provide ions for intercalation and deintercalation.^{37–41}

The o-MoO₃-based supercapacitors showed both a hybrid
battery-supercapacitor behavior demonstrating high energy
and power densities for transparent microsupercapacitors as
shown in the Ragone plot of Figure 12a obtained by direct
integration of the instantaneous power under the CV curve.

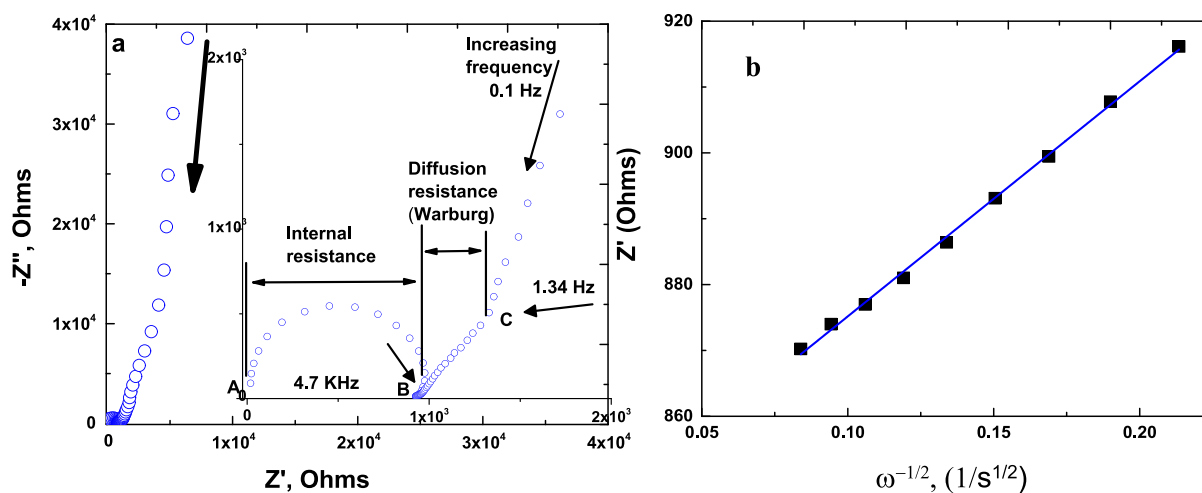


Figure 11. (a) A Nyquist plot of the transparent supercapacitor shows Z' behaving nearly parallel to the $-Z''$ axis approaching the theoretical limit of supercapacitor behavior. (b) The Warburg coefficient was calculated with a linear fit at low-frequency range (<25 kHz).

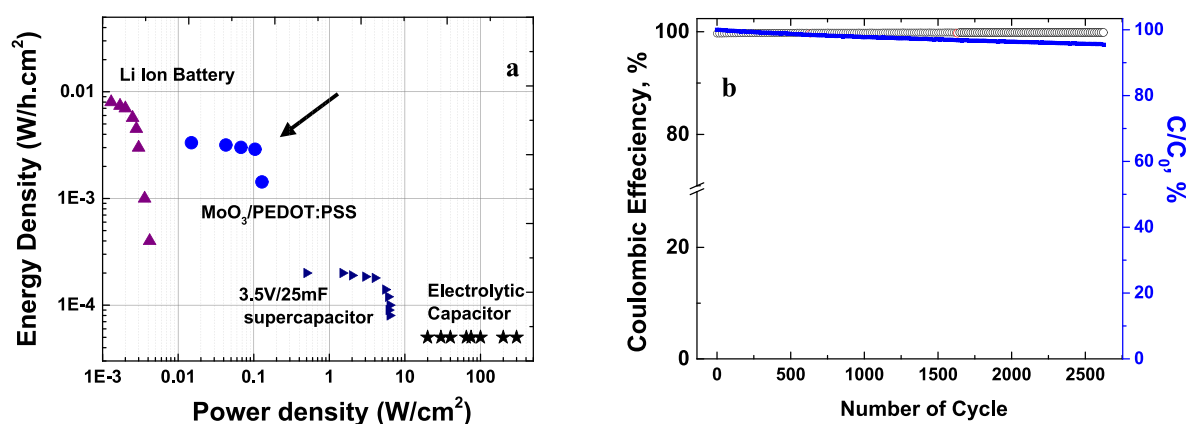


Figure 12. (a) A Ragone plot of areal energy density vs power density comparing transparent PEDOT:PSS/MoO₃/SA devices with Li ion batteries, electrolytic supercapacitors, and microsupercapacitors. (b) The Coulombic efficiency (○) and capacitance of the devices (■) vs number of cycles.

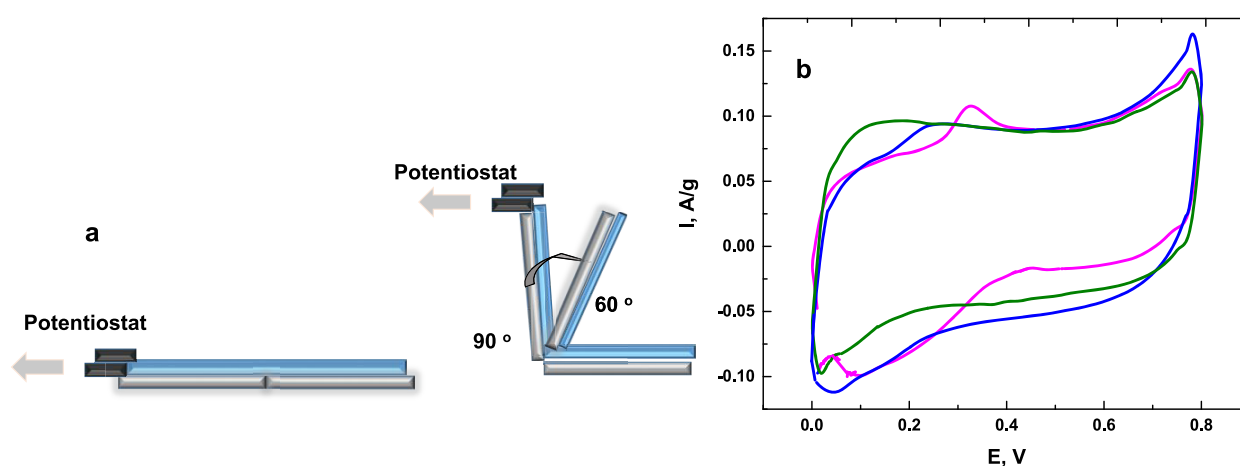


Figure 13. (a) Supercapacitor films were placed on a substrate and moved to 60° and 90° where measurements were performed while bending. (b) Cyclic voltammetry measurements of the MoO₃/PEDOT/PSS film supercapacitors at bending angles of 0°, 60°, and 90° at a scan rate of 5 mV/s.

504 The designed morphology of the PEDOT:PSS with the o-
 505 MoO₃ tunnel structure enables intercalation of protons (H⁺)
 506 from the sulfuric acid electrolyte which results in super-
 507 capacitors having high energy densities. The Coulombic
 508 efficiency measured over 2500 cycles (at 2.5 A/g) was 99.7%
 509 (Figure 12b), and the device exhibited excellent areal
 510 capacitance retention. Similar life cycles have been reported
 511 for complex redox-EDLC systems.^{57,58} Meanwhile, our device
 512 exhibits aerial capacitance up to 2.99 mF/cm²; flexible
 513 transparent supercapacitors of embedded PEDOT:PSS/
 514 AgNFs network exhibited areal capacitance of 0.91 mF/cm².⁵⁹
 515 Systems without transparency requirements are a different
 516 class of supercapacitors. Spicule-like Ni₃S₂ shells grown on
 517 molybdenum nanoparticle doped nickel foams are recently
 518 reported with 1.06 C cm² (361 C/g) at 1 mA/cm² and good
 519 rate capability.⁶¹ More recently, high-performance super-
 520 capacitors consisting of NiMoO₄ nanowire arrays and carbon
 521 nanotubes film have been reported to demonstrate 91.6%
 522 capacitance retention.⁶⁰⁻⁶² More recently, a range of super-
 523 capacitors with complex electrodes have been studied and
 524 reported.⁶³⁻⁶⁹

525 The transparent MoO₃/PEDOT:PSS/PET devices are
 526 completely flexible. The electrochemical performance of the
 527 devices was measured while under bending conditions at
 528 bending angles of 60° and 90°. The device was mounted on a
 529 two-piece flat substrate of equal lengths movable in specific

530 angles. These angles can also be measured by knowing triangle
 531 dimensions. The device was connected to the potentiostat
 532 where cyclic voltammetry was performed at 5 mV/s while
 533 bending at 60° and 90° angles. The excellent electrochemical
 534 performance nearly remained unchanged while bending
 535 f13

CONCLUSIONS

536
 537 In summary, high performance transparent (*T* > 70% at 550
 538 nm) supercapacitor/electrochromic devices have been fab-
 539 ricated by using PEDOT:PSS and 2D o-MoO₃ nanosheets as
 540 both pseudocapacitive and EDLC active materials. The
 541 exceptional performance is attributed to the high charge (H⁺,
 542 SO₄²⁻) storage capacity enabled by high surface area
 543 PEDOT:PSS doped with sulfuric acid facilitating proton
 544 intercalation/deintercalation into and out of o-MoO₃.
 545 PEDOT:PSS, an ionic and electronic conductor, acts both as
 546 an active layer storing ionic species and as a current collector.
 547 Upon application of a voltage, protons (H⁺) intercalate into o-
 548 MoO₃, resulting in a color change for this negative electrode.
 549 The positive electrode is designed to remain as a transparent
 550 window for the supercapacitor. This provides an opportunity
 551 to create charge storage devices with electrochromic
 552 functionality.

553 ■ ASSOCIATED CONTENT

554 ■ Supporting Information

555 The Supporting Information is available free of charge on the
556 ACS Publications website at DOI: 10.1021/acsaem.8b02258.

557 Characterizations (eqs S1–S6), dynamic light scattering
558 (Table S1), wide-angle X-ray scattering (Table S2 and
559 Figure S1), Raman Spectroscopy (Figure S2), cyclic
560 voltammetry of bending mode (Figure S3a and ac
561 impedance spectroscopy, Bode plot (Figure S3b) (PDF)

562 ■ AUTHOR INFORMATION

563 Corresponding Author

564 *E-mail: mitra.yoonessi@gmail.com.

565 ORCID 

566 Mitra Yoonessi: 0000-0002-0078-8999

567 Laurent Pilon: 0000-0001-9459-8207

568 Notes

569 The authors declare no competing financial interest.

570 ■ ACKNOWLEDGMENTS

571 The authors thank Professor Richard B. Kaner for his guidance
572 and generous support for this work to be accomplished. The
573 authors also thank Kimoto Tech Inc. for providing the
574 PEDOT:PSS/PET films. Funding for testing and character-
575 ization was provided by Nanotech Energy.

576 ■ REFERENCES

- 577 (1) Pech, D.; Brunet, M.; Durou, H.; Huang, P.; Mochalin, V.;
578 Gogotsi, Y.; Taberna, P.; Simon, P. Ultrahigh-Power Micrometre-
579 Sized Supercapacitors Based On Onion-Like Carbon. *Nat. Nano-*
580 *technol.* **2010**, *5*, 651–654.
- 581 (2) Gogotsi, Y. Materials Science: Energy Storage Wrapped Up.
582 *Nature* **2014**, *509*, 568–570.
- 583 (3) Yuan, Y.; Zhan, C.; He, K.; Chen, H.; Yao, W.; Sharifi-Asl, S.;
584 Song, B.; Yang, Z.; Nie, A.; Luo, X.; Wang, H.; Wood, S. M.; Amine,
585 K.; Islam, M. S.; Lu, J.; Shahbazian-Yassar, R. The Influence Of Large
586 Cations On The Electrochemical Properties Of Tunnel-Structured
587 Metal Oxides. *Nat. Commun.* **2016**, *7*, 13374.
- 588 (4) Kim, H.-S.; Cook, J. B.; Lin, H.; Ko, J. S.; Tolbert, S. H.; Ozolins,
589 V.; Dunn, B. Oxygen Vacancies Enhance Pseudocapacitive Charge
590 Storage Properties of MoO_{3-x}. *Nat. Mater.* **2017**, *16*, 45420.
- 591 (5) El-Kady, M. F.; Ihms, M.; Li, M.; Hwang, J. Y.; Mousavi, M. F.;
592 Chaney, L.; Lech, A. T.; Kaner, R. B. Engineering Three-Dimensional
593 Hybrid Supercapacitors And Microsupercapacitors For High-Perform-
594 ance Integrated Energy Storage. *Proc. Natl. Acad. Sci. U. S. A.* **2015**,
595 *112*, 4233–4238.
- 596 (6) Lee, G.; Kim, D.; Kim, D.; Oh, S.; Yun, J.; Kim, J.; Lee, S.-S.; Ha,
597 J. S. Fabrication of A Stretchable And Patchable Array Of High
598 Performance Micro-Supercapacitors Using A Non-Aqueous Solvent
599 Based Gel Electrolyte. *Energy Environ. Sci.* **2015**, *8*, 1764–1774.
- 600 (7) Lai, C.-H.; Ashby, D.; Moz, M.; Gogotsi, Y.; Pilon, L.; Dunn, B.
601 Designing Pseudocapacitance for Nb₂O₅/Carbide-Derived Carbon
602 Electrodes and Hybrid Devices. *Langmuir* **2017**, *33*, 9407–9415.
- 603 (8) Chen, L.-F.; Huang, Z.-H.; Liang, H.-W.; Yao, W.-T.; Yu, Z.-Y.;
604 Yu, S.-H. Flexible All-Solid-State High-Power Supercapacitor
605 Fabricated with Nitrogen-Doped Carbon Nanofiber Electrode
606 Material Derived from Bacterial Cellulose. *Energy Environ. Sci.* **2013**,
607 *6*, 3331–3338.
- 608 (9) Li, H.; Tao, Y.; Zheng, X.; Luo, J.; Kang, F.; Cheng, H.-M.; Yang,
609 Q.-H. Ultra-Thick Graphene Bulk Supercapacitor Electrodes for
610 Compact Energy Storage. *Energy Environ. Sci.* **2016**, *9*, 3135–3142.
- 611 (10) Lee, G.; Kim, D.; Kim, D.; Oh, S.; Yun, J.; Kim, J.; Lee, S.-S.;
612 Ha, J. S. Fabrication of a Stretchable and Patchable Array of High
613 Performance Micro-Supercapacitors Using a Non-Aqueous Solvent
614 Based Gel Electrolyte. *Energy Environ. Sci.* **2015**, *8*, 1764–1774.

- (11) Stoller, M. D.; Magnuson, C. W.; Zhu, Y.; Murali, S.; Suk, J. W.;
615 Piner, R.; Ruoff, R. S. Interfacial Capacitance of Single Layer
616 Graphene. *Energy Environ. Sci.* **2011**, *4*, 4685.
- (12) Su, Z.; Yang, C.; Xie, B.; Lin, Z.; Zhang, Z.; Liu, J.; Li, B.; Kang,
617 F.; Wong, C. P. Scalable Fabrication of MnO₂ Nanostructure
618 Deposited on Free-Standing Ni Nanocone Arrays for Ultrathin,
619 Flexible, High-Performance Micro-Supercapacitor. *Energy Environ. Sci.*
620 **2014**, *7*, 2652–2659.
- (13) Li, N.; Yang, G.; Sun, Y.; Song, H.; Cui, H.; Yang, G.; Wang, C.
621 Free-Standing and Transparent Graphene Membrane of Polyhedron
622 Box-Shaped Basic Building Units Directly Grown Using a NaCl
623 Template for Flexible Transparent and Stretchable Solid-State
624 Supercapacitors. *Nano Lett.* **2015**, *15*, 3195–3203.
- (14) Chen, T.; Xue, Y.; Roy, A. K.; Dai, L. Transparent and
625 Stretchable High-Performance Supercapacitors Based on Wrinkled
626 Graphene Electrodes. *ACS Nano* **2014**, *8*, 1039–1046.
- (15) Chen, F.; Wan, P.; Xu, H.; Sun, X. Flexible Transparent
627 Supercapacitors Based on Hierarchical Nanocomposite Films. *ACS*
628 *Appl. Mater. Interfaces* **2017**, *9*, 17865–17871.
- (16) Lee, H.; Hong, S.; Lee, J.; Suh, Y. D.; Kwon, J.; Moon, H.; Kim,
629 H.; Yeo, J.; Ko, S. H. Highly Stretchable and Transparent
630 Supercapacitor by Ag-Au Core-Shell Nanowire Network with High
631 Electrochemical Stability. *ACS Appl. Mater. Interfaces* **2016**, *8*, 15449–
632 15458.
- (17) Gao, Y.; Zhou, Y. S.; Xiong, W.; Jiang, L. J.; Mahjouri-Samani,
633 M.; Thirugnanam, P.; Huang, X.; Wang, M. M.; Jiang, L.; Lu, Y. F.
634 Transparent, Flexible, and Solid-State Supercapacitors Based on
635 Graphene Electrodes. *APL Mater.* **2013**, *1*, 012101.
- (18) Suktha, P.; Phattharasupakun, N.; Sawangphruk, M. Trans-
636 parent Supercapacitors of 2 Nm Ruthenium Oxide Nanoparticles
637 Decorated on a 3D Nitrogen-Doped Graphene Aerogel. *Sustainable*
638 *Energy & Fuels* **2018**, *2*, 1799–1805.
- (19) Li, N.; Huang, X.; Li, R.; Chen, Y.; Li, Y.; Shi, Z.; Zhang, H.
639 Pseudocapacitive Transparent/Flexible Supercapacitor Based on
640 Graphene Wrapped Ni(OH)₂ Nanosheet Transparent Film Produced
641 Using Scalable Bio-Inspired Methods. *Electrochim. Acta* **2016**, *219*,
642 61–69.
- (20) Song, W.; Zhu, J.; Gan, B.; Zhao, S.; Wang, H.; Li, C.; Wang, J.
643 Flexible, Stretchable, and Transparent Planar Microsupercapacitors
644 Based on 3D Porous Laser-Induced Graphene. *Small* **2018**, *14*,
645 1702249.
- (21) de Castro, I. A.; Datta, R. S.; Ou, J. Z.; Castellanos-Gomez, A.;
646 Sriram, S.; Daeneke, T.; Kalantar-Zadeh, K. Molybdenum Oxides -
647 From Fundamentals to Functionality. *Adv. Mater.* **2017**, *29*, 1701619.
- (22) Wang, Q. H.; Kalantar-Zadeh, K.; Kis, A.; Coleman, J. N.;
648 Strano, M. S. Electronics and Optoelectronics of Two-Dimensional
649 Transition Metal Dichalcogenides. *Nat. Nanotechnol.* **2012**, *7*, 699–
650 712.
- (23) Acerce, M.; Voiry, D.; Chhowalla, M. Metallic 1T Phase MoS₂
651 Nanosheets as Supercapacitor Electrode Materials. *Nat. Nanotechnol.*
652 **2015**, *10*, 313–318.
- (24) Huang, P.-R.; He, Y.; Cao, C.; Lu, Z.-H. Impact of Lattice
653 Distortion and Electron Doping on α -MoO₃ Electronic Structure. *Sci.*
654 *Rep.* **2015**, *4*, 7131.
- (25) Zhang, B. Y.; Zavabeti, A.; Chrimes, A. F.; Haque, F.; O'Dell, L.
655 A.; Khan, H.; Syed, N.; Datta, R.; Wang, Y.; Chesman, A. S. R.;
656 Daeneke, T.; Kalantar-Zadeh, K.; Ou, J. Z. Degenerately Hydrogen
657 Doped Molybdenum Oxide Nanodisks for Ultrasensitive Plasmonic
658 Biosensing. *Adv. Funct. Mater.* **2018**, *28*, 1706006.
- (26) Borgschulte, A.; Sambalova, O.; Delmelle, R.; Jenatsch, S.;
659 Hany, R.; Nüesch, F. Hydrogen Reduction of Molybdenum Oxide at
660 Room Temperature. *Sci. Rep.* **2017**, *7*, 40761.
- (27) Guo, Y.; Robertson, J. Origin of the High Work Function and
661 High Conductivity of MoO₃. *Appl. Phys. Lett.* **2014**, *105* (22),
662 222110.
- (28) Novoselov, K. S.; Geim, A. K.; Morozov, S. V.; Jiang, D.;
663 Katsnelson, M. I.; Grigorieva, I. V.; Dubonos, S. V.; Firsov, A. A. Two-
664 Dimensional Gas of Massless Dirac Fermions in Graphene. *Nature*
665 **2005**, *438*, 197–200.

- 684 (29) Sugimoto, W.; Ohnuma, T.; Murakami, Y.; Takasu, Y.
685 Molybdenum Oxide/Carbon Composite Electrodes as Electro-
686 chemical Supercapacitors. *Electrochem. Solid-State Lett.* **2001**, *4* (9),
687 A145.
- 688 (30) Zhou, K.; Zhou, W.; Liu, X.; Sang, Y.; Ji, S.; Li, W.; Lu, J.; Li,
689 L.; Niu, W.; Liu, H.; Chen, S. Ultrathin MoO₃/Nanocrystalsself-
690 Assembled on GrapheneNanosheets via Oxygen Bonding as Super-
691 capacitor Electrodes of High Capacitance and Long Cycle Life. *Nano*
692 *Energy* **2015**, *12*, 510–520.
- 693 (31) Yuksel, R.; Coskun, S.; Unalan, H. E. Coaxial Silver Nanowire
694 Network Core Molybdenum Oxide Shell Supercapacitor Electrodes.
695 *Electrochim. Acta* **2016**, *193*, 39–44.
- 696 (32) Giardi, R.; Porro, S.; Topuria, T.; Thompson, L.; Pirri, C. F.;
697 Kim, H.-C. One-Pot Synthesis of Graphene-Molybdenum Oxide
698 Hybrids and Their Application to Supercapacitor Electrodes. *Appl.*
699 *Mater. Today* **2015**, *1*, 27–32.
- 700 (33) Zhang, R.; Ding, J.; Liu, C.; Yang, E.-H. Highly Stretchable
701 Supercapacitors Enabled by Interwoven CNTs Partially Embedded in
702 PDMS. *ACS Appl. Energy Mat* **2018**, *1*, 2048–2055.
- 703 (34) Drozdov, A. D.; Christiansen, J. d.C. Modeling the Effects of
704 PH and Ionic Strength on Swelling of Anionic Polyelectrolyte Gels.
705 *Modell. Simul. Mater. Sci. Eng.* **2015**, *23* (5), 055005.
- 706 (35) Yu, H.; Wu, J.; Fan, L.; Lin, Y.; Xu, K.; Tang, Z.; Cheng, C.;
707 Tang, S.; Lin, J.; Huang, M.; Lan, Z. A Novel Redox-Mediated Gel
708 Polymer Electrolyte for High-Performance Supercapacitor. *J. Power*
709 *Sources* **2012**, *198*, 402–407.
- 710 (36) Volkov, A. V.; Wijeratne, K.; Mitraka, E.; Ail, U.; Zhao, D.;
711 Tybrandt, K.; Andreasen, J. W.; Berggren, M.; Crispin, X.;
712 Zozoulenko, I. V. Understanding the Capacitance of PEDOT:PSS.
713 *Adv. Funct. Mater.* **2017**, *27*, 1700329.
- 714 (37) Fong, K. D.; Wang, T.; Kim, H.-K.; Kumar, R. V.; Smoukov, S.
715 K. Semi-Interpenetrating Polymer Networks for Enhanced Super-
716 capacitor Electrodes. *ACS Energy Lett.* **2017**, *2*, 2014–2020.
- 717 (38) Kim, N.; Kee, S.; Lee, S. H.; Lee, B. H.; Kahng, Y. H.; Jo, Y.-R.;
718 Kim, B.-J.; Lee, K. Highly Conductive PEDOT:PSS Nanofibrils
719 Induced By Solution-Processed Crystallization. *Adv. Mater.* **2014**, *26*,
720 2268–2272.
- 721 (39) Rivnay, J.; Inal, S.; Collins, B. A.; Sessolo, M.; Stavrinidou, E.;
722 Strakosas, X.; Tassone, C.; DeLongchamp, D. M.; Malliaras, G. G.
723 Structural Control of Mixed Ionic and Electronic Transport in
724 Conducting Polymers. *Nat. Commun.* **2016**, *7*, 11287.
- 725 (40) Gomes, L.; Branco, A.; Moreira, T.; Feliciano, F.; Pinheiro, C.;
726 Costa, C. Increasing the Electrical Conductivity of Electrochromic
727 PEDOT:PSS Films - A Comparative Study. *Sol. Energy Mater. Sol.*
728 *Cells* **2016**, *144*, 631–640.
- 729 (41) Wang, K.; Wu, H.; Meng, Y.; Zhang, Y.; Wei, Z. Integrated
730 Energy Storage and Electrochromic Function in One Flexible Device:
731 An Energy Storage Smart Window. *Energy Environ. Sci.* **2012**, *5*, 8384.
- 732 (42) Yang, X.; Zhu, G.; Wang, S.; Zhang, R.; Lin, L.; Wu, W.; Wang,
733 Z. L. A Self-Powered Electrochromic Device Driven by a Nano-
734 generator. *Energy Environ. Sci.* **2012**, *5*, 9462.
- 735 (43) Yang, P.; Sun, P.; Mai, W. Electrochromic Energy Storage
736 Devices. *Mater. Today* **2016**, *19*, 394–402.
- 737 (44) Cai, G.; Darmawan, P.; Cui, M.; Wang, J.; Chen, J.; Magdassi,
738 S.; Lee, P. S. Highly Stable Transparent Conductive Silver Grid/
739 PEDOT:PSS Electrodes for Integrated Bifunctional Flexible Electro-
740 chromic Supercapacitors. *Adv. Energy Mater.* **2016**, *6*, 1501882.
- 741 (45) Andersson, G.; Magneli, A.; et al. On the Crystal Structure of
742 Molybdenum Trioxide. *Acta Chem. Scand.* **1950**, *4*, 793–797.
- 743 (46) Yang, X.; Zhu, G.; Wang, S.; Zhang, R.; Lin, L.; Wu, W.; Wang,
744 Z. L. A Self-Powered Electrochromic Device Driven by a Nano-
745 generator. *Energy Environ. Sci.* **2012**, *5*, 9462–9466.
- 746 (47) Bragg, S. L.; Phillips, D. C.; Lipson, H. *The Development of X-*
747 *ray Diffraction* (reprint of the G. Bell and Sons (London) ed. of
748 1975); Dover Publications: NewYork, 1992.
- 749 (48) Nguyen, D.-T.; Vedraïne, S.; Cattin, L.; Torchio, P.; Morsli, M.;
750 Flory, F.; Bernède, J. C. Effect of the Thickness of the MoO₃ Layers
751 on Optical Properties of MoO₃/Ag/MoO₃ Multilayer Structures. *J.*
752 *Opt. Phys.* **2012**, *112*, 063505.
- (49) Du, Y.; Li, G.; Peterson, E. W.; Zhou, J.; Zhang, X.; Mu, R.; 753
Dohnálek, Z.; Bowden, M.; Lyubinsky, I.; Chambers, S. A. Iso- 754
Oriented Monolayer α -MoO₃ (010) Films Epitaxially Grown on 755
SrTiO₃ (001). *Nanoscale* **2016**, *8* (5), 3119–3124. 756
- (50) Arora, P. Electrochemical Investigations of Cobalt-Doped 757
LiMn₂O₄ as Cathode Material for Lithium-Ion Batteries. *J. Electro-* 758
chem. Soc. **1998**, *145*, 807. 759
- (51) Bagotsky, V. S.; Skundin, A. M.; Volfkovich, Y. M. *Electrochem.* 760
Power Sources. In The Electrochemical Society Series; John Wiley & 761
Sons: Hoboknan, NJ, 2015. 762
- (52) Mai, L.-Q.; Minhas-Khan, A.; Tian, X.; Hercule, K. M.; Zhao, 763
Y.-L.; Lin, X.; Xu, X. Synergistic Interaction between Redox-Active 764
Electrolyte and Binder-Free Functionalized Carbon for Ultrahigh 765
Supercapacitor Performance. *Nat. Commun.* **2013**, *4*, 2923. 766
- (53) DeLongchamp, D.; Hammond, P. T. Layer-by-Layer Assembly 767
of PEDOT/PolyanilineElectrochromic Devices. *Adv. Mater.* **2001**, *13*, 768
1455–1459. 769
- (54) Lindström, H.; Södergren, S.; Solbrand, A.; Rensmo, H. akan; 770
Hjelm, J.; Hagfeldt, A.; Lindquist, S.-E. Li⁺ Ion Insertion in TiO₂ 771
(Anatase). 2. Voltammetry on Nanoporous Films. *J. Phys. Chem. B* 772
1997, *101*, 7717–7722. 773
- (55) Girard, H.-L.; Wang, H.; d'Entremont, A.; Pilon, L. Physical 774
Interpretation of Cyclic Voltammetry for Hybrid Pseudocapacitors. *J.* 775
Phys. Chem. C **2015**, *119*, 11349–11361. 776
- (56) Chen, T.; Peng, H.; Durstock, M.; Dai, L. High-Performance 777
Transparent and Stretchable All-Solid Supercapacitors Based on 778
Highly Aligned Carbon Nanotube Sheets. *Sci. Rep.* **2015**, *4*, 3612. 779
- (57) Jiang, H.; Ma, H.; Jin, Y.; Wang, L.; Gao, F.; Lu, Q. Hybrid α - 780
Fe₂O₃@Ni(OH)₂Nanosheet Composite for High-Rate-Performance 781
Supercapacitor Electrode. *Sci. Rep.* **2016**, *6*, 31751. 782
- (58) Sui, L.; Tang, S.; Dai, Z.; Zhu, Z.; Huangfu, H.; Qin, X.; Deng, 783
Y.; Haarberg, G. M. Supercapacitive Behavior of an Asymmetric 784
Supercapacitor Based on a Ni(OH)₂/XC-72 Composite. *New J. Chem.* 785
2015, *39*, 9363–9371. 786
- (59) Singh, S. B.; Kshetri, T.; Singh, T. I.; Kim, N. H.; Lee, J. H. 787
Embedded PEDOT:PSS/AgNFs Network Flexible Transparent 788
Electrode For Solid-State Supercapacitor. *Chem. Eng. J.* **2019**, *359*, 789
197–207. 790
- (60) Cheng, Y.; Zhai, M.; Guo, M.; Yu, Y.; Hu, J. A Novel Electrode 791
for Supercapacitors: Spicules-Like Ni₃S₂ Shell Grown On Molybde- 792
num Nanoparticles Doped Nickel Foam. *Appl. Surf. Sci.* **2019**, *467*, 793
1113–1121. 794
- (61) Maheswari, N.; Muralidharan, G. Controlled Synthesis of 795
Nanostructured Molybdenum Oxide Electrodes for High Perform- 796
ance Supercapacitor Devices. *Appl. Surf. Sci.* **2017**, *416*, 461–469. 797
- (62) Zhang, S.-W.; Yin, B.-S.; Liu, C.; Wang, Z.-B.; Gu, D.-M. 798
NiMoO₄Nanowire Arrays And Carbon Nanotubes Film As Advanced 799
Electrodes For High-Performance Supercapacitor. *Appl. Surf. Sci.* **2000** 800
2018, *458*, 478–488. 801
- (63) Shafi, P. M.; Ganesh, V.; Bose, A. C. LaMnO₃/RGO/PANI 802
Ternary Nanocomposites for Supercapacitor Electrode Application 803
and Their Outstanding Performance in All-Solid-State Asymmetrical 804
Device Design. *ACS Appl. Energy Mater.* **2018**, *1*, 2802–2812. 805
- (64) Hou, X.; Zhang, Y.; Dong, Q.; Hong, Y.; Liu, Y.; Wang, W.; 806
Shao, J.; Si, W.; Dong, X. Metal Organic Framework Derived Core- 807
Shell Structured Co₉S₈@N-C@MoS₂ Nanocubes for Supercapacitor. 808
ACS Appl. Energy Mater. **2018**, *1*, 3513–3520. 809
- (65) Kumar, L.; et al. Faster Ion Switching NiCo₂O₄ Nanoparticle 810
Electrode-Based Supercapacitor Device with High Performances and 811
Long Cycling Stability. *ACS Appl. Energy Mater.* **2018**, *1*, 6999–7006. 812
- (66) Wang, N.; Wang, Y.; Cui, S.; Hou, H.; Mi, L.; Chen, W. A 813
Hollow Tube-on-Tube Architecture of Carbon-Tube-Supported 814
Nickel Cobalt Sulfide Nanotubes for Advanced Supercapacitors. 815
ChemNanoMat **2017**, *3*, 269–276. 816
- (67) Wang, G.; Zhang, M.; Lu, Lu; Xu, H.; Xiao, Z.; Liu, S.; Gao, S.; 817
Yu, Z. One-Pot Synthesis of CuS Nanoflower-Decorated Active 818
Carbon Layer for High-Performance Asymmetric Supercapacitors. 819
CHEMNANOMAT **2018**, *4*, 964–971. 820

- 821 (68) Liu, T.; Zhang, L.; Cheng, B.; You, W.; Yu, J. Fabrication Of A
822 Hierarchical NiO/C Hollow Sphere Composite And Its Enhanced
823 Supercapacitor Performance. *Chem. Commun.* **2018**, *54*, 3731–3734.
- 824 (69) Balogun, M.-S.; Huang, Y.; Qiu, W.; Yang, H.; Ji, H.; Tong, Y.
825 Updates on the development of nanostructured transition metal
826 nitrides for electrochemical energy storage and water splitting. *Mater.*
827 *Today* **2017**, *20*, 425–451.